

## Reply to Reviewer 1

Thanks for the thorough review! We have corrected all the minor issues as suggested by the reviewer (they appear in the revised version attached at the end).

Here we provide a reply to the major points raised by the reviewer (highlighted in red).

A point made by the Authors is the limited amount of spatial variability of the input data (due to the smearing and coarse horizontal sampling of satellite and reanalysis data), and thereby a possible under-estimation of NUBF and wind shear errors. Since, NUBF and wind shear biases are mostly sub-footprint effects, I was wondering if there was any merit in spatially interpolating (if possible with an order higher than linear) the input data (satellite, ECMWF) to a finer resolution, before computing the Doppler velocity errors?

The reviewer is right in pinpointing at the sub-footprint variability as the key source of NUBD and wind shear errors. Part of this is certainly captured by the variability in our datasets but as mentioned in our conclusions (point 1 page 19) it is not trivial to downscale reflectivity and wind fields to a finer resolution. This is left for future studies.

P9L10-13: For attenuation, do the Authors 1) correct for attenuation in the CloudSat viewing configuration (using the 2C-RAIN products?), 2) generate unattenuated Z in the WIVERN look direction (and resolution), and 3) add attenuation in the WIVERN viewing direction?

- If not, how much of a limiting factor is it for the realism of your simulations, especially for large off-nadir look angles?
- If so, then regions with invalid radar data aloft (due to attenuation or multiple scattering) would invalidate radar data in their “shadow” to the surface (along the viewing direction). This limits the amount of radar data available for the statistical analysis. Could you assess/comment on the penalty incurred by this effect?

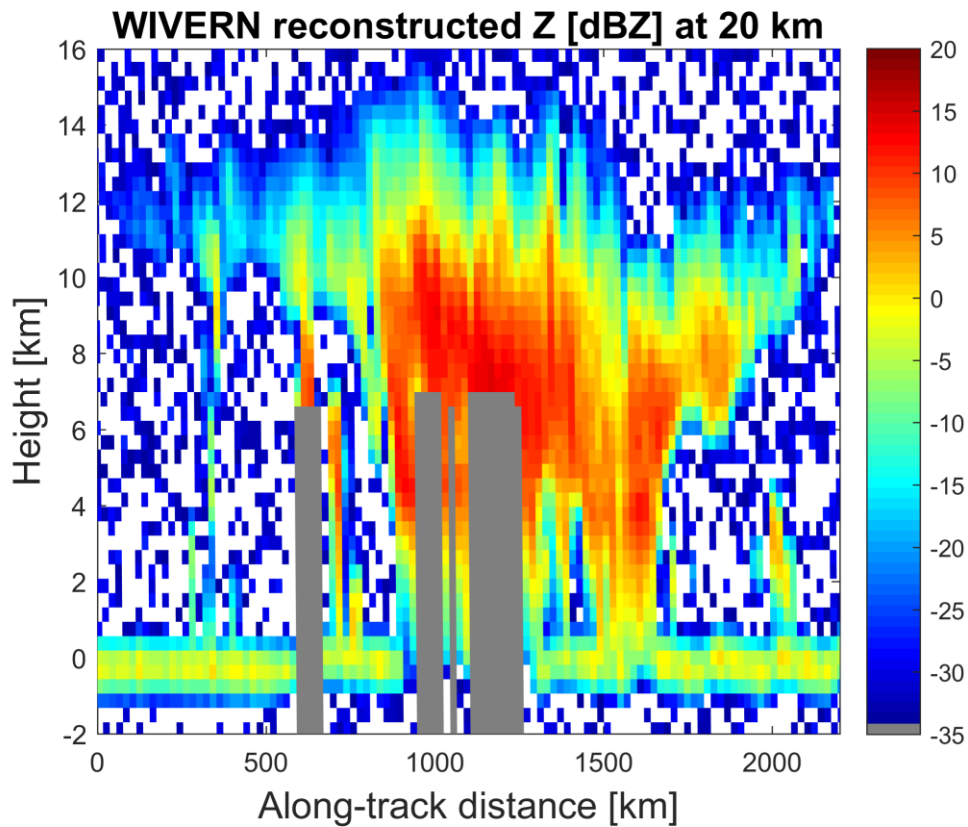
We do correct for attenuation as the reviewer suggests. Indeed the reason for using the 2C-RAIN product is to get reconstructions of profiles of unattenuated reflectivities and of attenuation that can be used for reconstructing the view at 41 degree incidence angle. Text at page 9 has been modified. The 2C-RAIN product does not produce a result in presence of strong attenuation and/or multiple scattering. For these areas we assume that a shadow region will propagate from an altitude equal to the freezing level height +2km. These shadowed regions are those grey shaded in Fig6. This represents less than 5% of the CloudSat data.

P12L7-9: Wouldn't the dominant contribution come from the vertical only if the look angle exceed 45 degrees? It seems to me that more than a “dominant factor”, the key here is that, for non-nadir look angles, the gradient in the direction orthogonal to the Boresight (“eta”) becomes correlated to the vertical gradient. Please clarify.

Well, generally speaking, vertical gradients of reflectivities are much larger than horizontal ones. As a result, even if the incidence angle is not exceeding 45degrees, the vertical reflectivity gradients have a larger impact onto NUBF effects. We have rephrased the statement to make this clear.

P15L22-33: For a pulse-pair radar, the noisiness would be injected when building the (I,Q) voltage samples, and this noisiness would affect both reflectivity and velocity (Approach described in Zrnic 1975 or Sirmans and Baumgartner 1975). Is your addition of noise to the WIVERN Doppler data consistent with the (I,Q)-based approach?

Yes the procedure is similar to the one for a pulse-pair radar, so indeed the noisiness affects both reflectivities and velocities. We realised that in the current version the left panel of Fig.6 represents indeed the 5-km ideal reflectivity field (i.e. the one computed from the CloudSat reflectivities before injecting the noise appropriate for a system with single pulse sensitivity of -19 dBZ). In the revised version we will include the 20-km reflectivity field after noise subtraction (see attached). Note that in this situation we can get reflectivities down to -32.5 dBZ because 20 km integration corresponds to 520 pulses.



We will put this figure in the updated version.

*P16, Fig 11: Errors reported in terms of standard deviation, wouldn't it be better to express them in terms of RMSE, which would account for effects of biases; That would maybe also help the reader understand Fig.11 ...*

*The figure has been changed and everything has been plotted in terms of RMSE. The text commenting the figure has been changed. .*

*o Do the Authors have recommendations for a better correction of wind-shear-induced errors over a wider range of SNR values?*

*No we do not see any method to correct for it. But such error remains small compared to the other errors involved in such measurement.*

*A revised version with all correction in place is attached.*

# Doppler W-band polarization diversity spaceborne radar simulator for wind studies

Alessandro Battaglia<sup>1,2</sup>, Ranvir Dhillon<sup>1</sup>, and Anthony Illingworth<sup>3</sup>

<sup>1</sup>University of Leicester, UK

<sup>2</sup>National Centre for Earth Observation, UK

<sup>3</sup>University of Reading, UK

**Correspondence:** Alessandro Battaglia

ab474@le.ac.uk

**Abstract.** CloudSat observations are used in combination with collocated European Centre for Medium-Range Weather Forecasts (ECMWF) reanalysis to simulate spaceborne W-band Doppler observations from slant-looking radars. The simulator also includes cross-polarization effects which are relevant if the Doppler velocities are derived from polarization diversity pulse pair correlation. A specific conically scanning radar configuration (“WIVERN”), recently proposed to the ESA-Earth Explorer 5 10 call that aims to provide global in-cloud winds for data assimilation, is analysed in detail in this study.

One hundred granules of CloudSat data are exploited to investigate the impact on Doppler velocity estimates from three specific effects: (1) non-uniform beam filling, (2) wind shear, and (3) cross talk between orthogonal polarization channels induced by hydrometeors and surface targets. Errors associated with non-uniform beam filling constitute the most important source of error and can account for almost  $1 \text{ m s}^{-1}$  standard deviation, but this can be reduced effectively to less than  $0.5 \text{ m s}^{-1}$  10 by adopting corrections based on estimates of vertical reflectivity gradients. Wind-shear-induced errors are generally much smaller ( $\sim 0.2 \text{ m s}^{-1}$ ). A methodology for correcting such errors has been developed based on estimates of the vertical wind shear and the reflectivity gradient. Low signal-to-noise ratios lead to higher random errors (especially in winds) and therefore the correction (particularly the one related to the wind-shear induced error) is less effective at low signal-to-noise ratio. Both errors can be underestimated in our model because the CloudSat data do not fully sample the spatial variability of the reflectivity 15 fields whereas the ECMWF reanalysis may have smoother velocity fields than in reality (e.g. they underestimate vertical wind shear).

The simulator allows quantification of the average number of accurate measurements that could be gathered by the Doppler radar for each polar orbit, which is strongly impacted by the selection of the polarization diversity  $H - V$  pulse separation,  $T_{hv}$ . For WIVERN a selection close to  $20 \mu\text{s}$  (with a corresponding folding velocity equal to  $40 \text{ m s}^{-1}$ ) seems to achieve the 20 right balance between maximizing the number of accurate wind measurements (exceeding 10% of the time at any particular level in the mid-troposphere), and minimizing aliasing effects in the presence of high winds.

The study lays the foundation for future studies towards a thorough assessment of the performance of polar orbiting wide-swath W-band Doppler radars on a global scale. The next generation of scanning cloud radar systems and reanalyses with improved resolution will enable a full capture of the spatial variability of the cloud reflectivity and the in-cloud wind fields, 25 thus refining the results of this study.

## 1 Introduction

Observation of atmospheric 3D winds and their monitoring at multiple temporal and spatial scales has been identified as a priority in the recent NASA Decadal Survey (The Decadal Survey, 2017). Large-scale winds are paramount in the transport of energy and water through the atmosphere and, together with vertical motions of convection, are the main driver in controlling water vapor transport around the globe. They are an essential element in the circulation of the atmosphere, in coupling clouds and the general circulation, in understanding the hydrological cycle and in untangling climate challenges (Bony et al., 2015).

Zeng et al. (2016) state that “it is important to avoid all-or-nothing strategies for three-dimensional (3D) wind vector measurements”, i.e. that progress can be achieved with observing strategies that are not comprehensive - e.g. are only effective in certain conditions (clear sky, cloudy, etc.) and maybe capable of measuring only one or two components of the wind- and that complement each other. An integrated approach of active sensing (lidar, radar, scatterometer) and passive imagery or radiometry-based atmospheric motion vectors is therefore envisaged for improving global observations of winds in the future. In this synergistic approach, active sensors on LEO satellites could be used to calibrate observations from geostationary satellites that have excellent temporal coverage but are affected by large errors in assigning a height to the retrieved wind. Profiles of tropospheric winds currently have the highest priority (“the holy grail”) for all operational weather agencies. Doppler active sensors (lidars and radars) on LEO satellites which use atmospheric targets as wind tracers are unanimously credited to be the key instruments to achieve this priority. While an explorer/incubation mission of this type is recommended by NASA for the next decade (The Decadal Survey, 2017), the ESA Earth Explorer programme already has two missions in the pipeline aiming towards this goal. The ESA Aeolus mission to be launched in mid-2018 (Stoffelen et al., 2005) will provide the first Doppler lidar measurements of the line-of-sight winds in clear air and thin ice clouds. It will be followed by the ESA-JAXA Earth-CARE mission (launch planned for 2020, Illingworth et al. (2015)) that will provide vertical velocities of cloud particles via a nadir-pointing Doppler W-band radar. For the first time sedimentation rates of ice crystals (Kollias et al., 2014) and convective up- and down-draughts (Battaglia et al., 2011) will be observed from space.

However, none of these missions will be able to provide horizontal winds in deep cloud systems. McNally (2002) showed that “sensitive” areas where observations have the largest potential to improve forecasts are often cloudy. The nexus between clouds and winds is revealed in Fig. 1, a snapshot of the global winds and ice water content (IWC) at a height of 8 km from the European Centre for Medium-Range Weather Forecasts (ECMWF) model for 12 noon on 12 January 2018. Particularly obvious are the high values of IWC and rapidly changing winds associated with the storm to the south of Japan, as is the case for other mid-latitude depressions. Areas where winds change rapidly are often associated with clouds, and only radars can penetrate such areas.

Recent European Space Agency (ESA)-funded studies suggested addressing this wind observational gap by using W-band radars - ideal for their high sensitivity and narrow beamwidths - with scanning and Doppler capabilities. Both a stereoradar and a conically scanning configuration have been proposed (Battaglia and Kollias, 2014a; Illingworth et al., 2018a). The former investigates the link between microphysical and dynamical structures of cloud systems, including convective systems, while the latter, known as WInd VELOCITY Radar Nephoscope (WIVERN), aims to provide global in-cloud winds for data assimilation

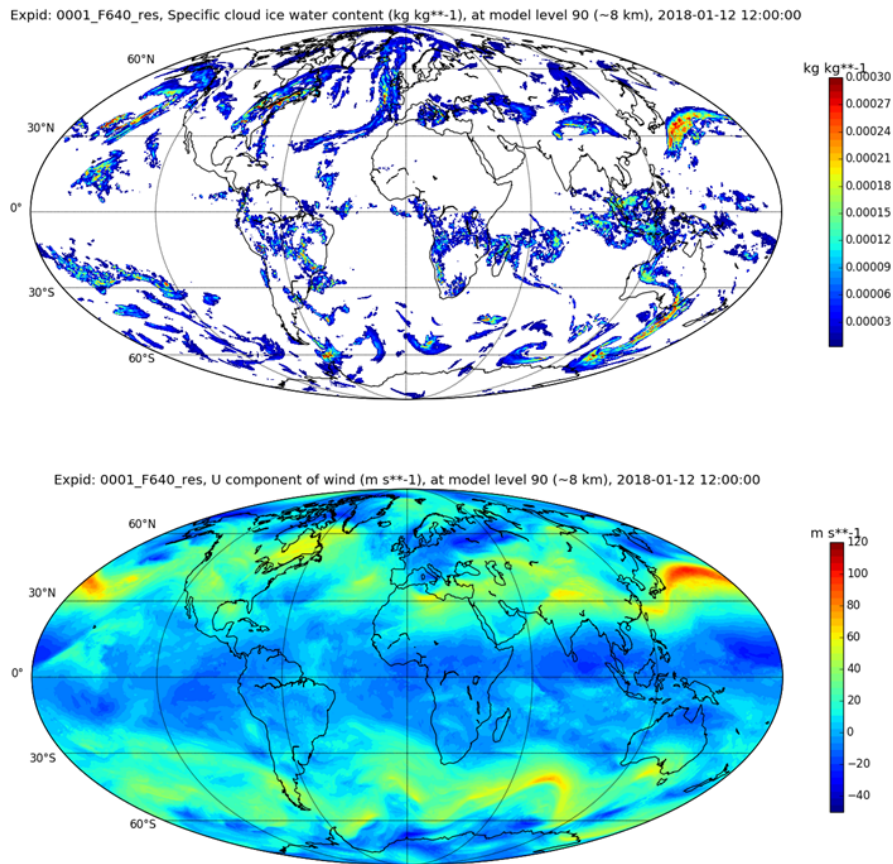


**Figure 1.** Cloud ice water content (top) and ECMWF zonal winds (bottom) at a height of 8 km at noon on 2018-01-02. The data are plotted at a resolution of about 14 km. Ice water is only plotted when the mixing ratio exceeds  $10^{-6}$  kg kg<sup>-1</sup> or  $\sim 2 \times 10^{-3}$  gm<sup>-3</sup> or a reflectivity of  $\sim 23$  dBZ (Hogan et al., 2006). Plot courtesy of M. Rennie, ECMWF.

and has now been proposed to the ESA Earth Explorer 10 call (Illingworth et al., 2018b). By conically scanning an 800 km wide ground track the radar allows the measurement of large-scale winds associated with long-lived systems to be assimilated into weather forecast models with daily coverage at mid-latitudes.

The commonalities of both systems are:

- they look/scan at a slant view (incidence angles in the range between 40° to 50°) in order to capture horizontal winds;
- 5 – they adopt polarization diversity to overcome the range-Doppler dilemma and to cope with the short decorrelation times associated with the Doppler fading inherent to millimetre Doppler radars on fast-moving low Earth orbiting satellites (Tanelli et al., 2002; Kollias et al., 2014);

- they require large antennas to achieve narrow ( $<\sim 0.1^\circ$ ) antenna beamwidth and thus to optimize the Doppler quality.

By focusing on slant-looking Doppler radars adopting polarization diversity this study aims to define a simulation framework which enables the assessment of radar performance on a global scale.

Doppler velocity accuracy requirements depend on the application but the WMO requirement for assimilating winds is to have errors lower than  $2 \text{ m s}^{-1}$  at a horizontal sampling of 50 km and a vertical resolution of 1 km or better (see Illingworth et al. (2018a) for a thorough discussion of wind user requirements). Noticeably Horanyi et al. (2014) state that assimilating winds with biases of  $1\text{-}2 \text{ m s}^{-1}$  can actually degrade the forecast. It is therefore important to assess the accuracy and precision of Doppler velocities for future spaceborne wind-observing radars. There are several sources of uncertainty associated with polarization diversity Doppler measurements from space, such as errors linked to non-uniform beam filling (NUBF) (Tanelli et al., 2002) coexisting with or without wind shear, cross talk between the H and V returns (Pazmany et al., 1999; Illingworth et al., 2018a; Wolde et al., 2018), clutter contamination, aliasing (Battaglia et al., 2013; Sy et al., 2013), mispointing (Tanelli et al., 2005; Battaglia and Kollias, 2014b), multiple scattering (Battaglia and Tanelli, 2011) and errors related to the Doppler estimators in the pulse-pair processing. The uncertainties associated with the pulse-pair processing are very well characterized: they depend on the signal-to-noise ratio (SNR), the radar Doppler spectral width, and the number of averaged samples (Doviak and Znić, 1993; Battaglia et al., 2013; Illingworth et al., 2018a). The other errors are more complicated and are generally assessed via simulations of cloud-resolving model scenes (Battaglia et al., 2013; Leinonen et al., 2015). In other cases, in order to avoid the uncertainties associated with transforming bulk microphysical properties to radar reflectivities, ground-based (Kollias et al., 2014; Burns et al., 2016) or aircraft (Sy et al., 2013, 2014) observations at the same radar frequency are exploited, with the advantage of reproducing naturally observed fields of reflectivity, together with their spatial variability. On the other hand such observations are seldom representative of the global scale. In addition only Battaglia et al. (2013) and Battaglia and Kollias (2014a) have addressed issues related to polarization diversity in a simulation framework.

In this study we exploit CloudSat W-band radar observations (Tanelli et al., 2008) in combination with collocated ECMWF wind reanalysis to simulate spaceborne W-band Doppler radar observations from off-nadir scanning radars. The simulator also includes cross-polarization induced by atmospheric targets in order to assess its impact on Doppler polarization diversity pulse-pair estimates. The proposed simulation framework can therefore enable an error budget assessment on a global scale for a satellite mission adopting a sun-synchronous orbit similar to CloudSat. Sect. 2 provides information about the datasets that have been used while Sect. 3 describes the Doppler radar simulator and its application to the case study of hurricane Igor. In Sect. 4  $\sim 100$  orbits of CloudSat data are exploited to characterize the performance of a W-band Doppler system on a global scale. Conclusions and future work are presented in Sect. 5.

## 2 Datasets

In order to simulate realistic scenes for assessing the capabilities of future spaceborne W-band Doppler radars, two ingredients are needed: (1) W-band reflectivity profiles through a variety of cloud regimes with spatial resolutions comparable or better

than those to be simulated and capable of representing the natural variability, and (2) wind profiles for the whole troposphere. In this work the former are taken from the CloudSat W-band radar, and the latter are extracted from ECMWF products.

## 2.1 CloudSat products

10 The CloudSat 94 GHz (3.2 mm) Cloud Profiling Radar (CPR) measures reflectivities from cloud- and precipitation-sized particles at a vertical resolution of 480 m for a cross-track/along-track horizontal footprint of  $1.5 \text{ km} \times 2.5 \text{ km}$  (Stephens et al., 2008). The radar has been collecting data on a polar sun-synchronous orbit since its launch in 2006 (Tanelli et al., 2008). This study makes use of different Level 2 CloudSat data products: the 2B-GEOPROF (Mace et al., 2007), the 2B-CLDCLASS-LIDAR (Sassen et al., 2008) and the 2C-RAIN-PROFILE (Haynes et al., 2009) (more details at <http://www.cloudsat.cira.colostate.edu/>).

## 15 2.2 ECMWF product

The European Centre for Medium-Range Weather Forecasts (ECMWF) maintains an archive of meteorological and air-quality data - covering a wide range of parameters including, for example, gas and pollutant concentrations, precipitation measurements and wind values - central to its core mission of producing numerical weather forecasts and monitoring the Earth system (<https://www.ecmwf.int/>).

20 For the study covered here, ECMWF global wind fields (u- and v-components) at a temporal resolution of 6 hours and latitude and longitude resolutions of  $0.1^\circ$  are used. The wind fields are provided at 25 pressure levels ranging from 1 to 1000 hPa. They are collocated with the CloudSat measurements by selecting the nearest ECMWF grid point (latitude and longitude) to the CloudSat position and by temporally interpolating to each CloudSat profile time stamp between the two closest ECMWF time stamps.

## 25 3 Simulator

### 3.1 Radar configuration

The radar configuration that will be used throughout this paper is the one depicted in Fig. 2. The radar specifications are detailed in Tab. 1. The configuration corresponds to the one proposed for the WIVERN mission (which involves a conically scanning system) when the antenna is looking in the same direction as the spacecraft motion (Illingworth et al., 2018a, b) and is very similar to the one proposed in Battaglia and Kollias (2014a). Therefore, we will refer to it as the “WIVERN forward” configuration. The antenna pattern is assumed Gaussian with a two-way gain equal to:

$$G^2(\theta) = G_0^2 \exp \left[ -8 \log(2) \left( \frac{\theta}{\theta_{3dB}} \right)^2 \right], \quad (1)$$

where  $G_0$  is the antenna gain in the boresight direction,  $\theta$  is the antenna polar angle with respect to the boresight and  $\theta_{3dB}$  is the antenna 3-dB beamwidth. The radar reflectivity and Doppler Doppler velocity are computed as:

$$5 \quad v_D(r) = \frac{\iiint_V v_r Z_m G^2 dV}{\iiint_V Z_m G^2 dV} \quad (2)$$

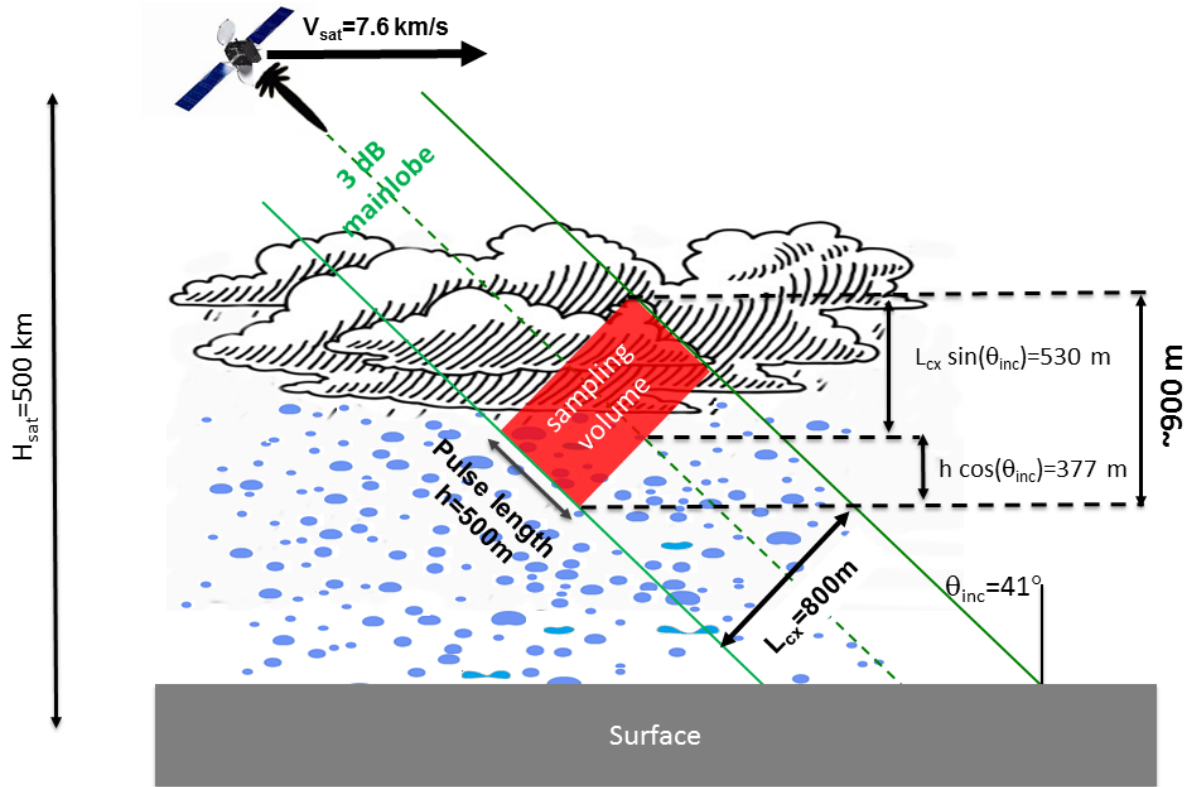


**Figure 2.** Schematic illustrating the geometry of a radar observing cloud and precipitation at a slant angle. The specifics of the radar are detailed in Tab. 1

where  $V$  is the backscattering volume (red box in Fig. 2),  $v_r$  is the wind velocity along the line of sight and  $Z_m$  is the measured reflectivity (generally variable within the backscattering volume). Since CloudSat only provides a 2D-curtain through cloud systems, the integral in Eq. (2) is reduced to a two-dimensional integral that can be performed in polar coordinates.

### 3.2 Case study: Hurricane Igor

- 10 The simulator rationale is demonstrated for a case study based on a CloudSat overpass over Hurricane Igor. Hurricane Igor originated from a broad area of low pressure that moved off the Cape Verde Islands on September 6, 2010. It subsequently developed into a tropical depression on September 8 and reached Category 4 status on September 12 with winds peaking at  $70 \text{ m s}^{-1}$ . CloudSat in ascending orbit overpassed to the East of the storm centre on September 16<sup>1</sup> when Igor had gradually

<sup>1</sup>Visit [http://cloudsat.atmos.colostate.edu/news/2010\\_atlantic](http://cloudsat.atmos.colostate.edu/news/2010_atlantic).

**Table 1.** Specifics of the radar for the simulation. The configuration here adopted is the one proposed for WIVERN in a recent ESA Earth Explorer 10 call.

Satellite altitude, $h_{sat}$	500 km
Satellite velocity, $v_{sat}$	$7600 \text{ ms}^{-1}$
Incidence angle, $\theta_i$	$41^\circ$
RF output frequency	94.05 GHz
Pulse width	$3.3 \mu\text{s}$
Antenna beamwidth, $\theta_{3dB}$	$0.07^\circ$
Transmit polarization	H or V
Cross-polarization	$< -25 \text{ dB}$
Single pulse sensitivity	$-19 \text{ dBZ}$
H-V Pair Repetition Frequency	4 kHz
Footprint speed	$300 \text{ kms}^{-1}$
Number of H-V Pairs per 1 km integration length	10

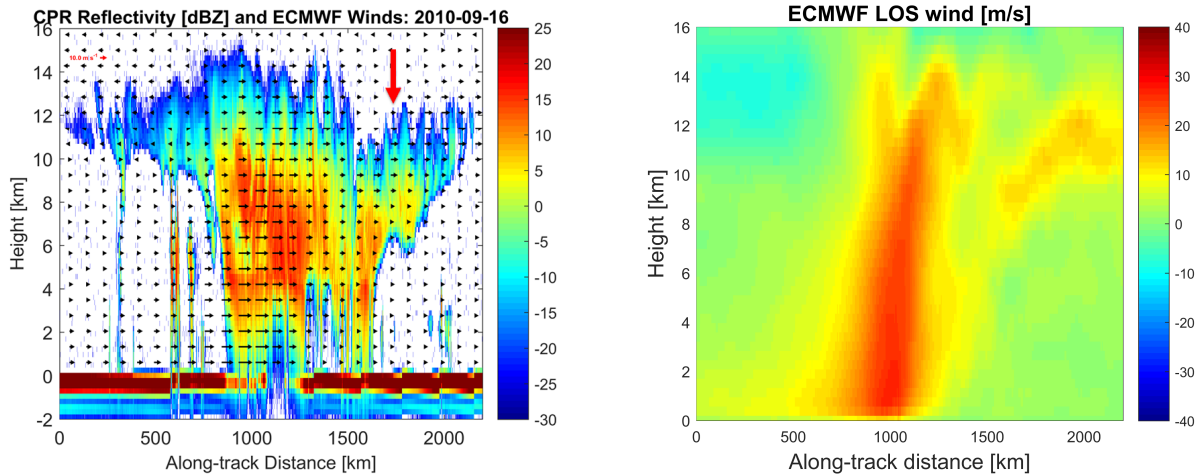


**Figure 3.** Left panel: CloudSat radar vertical reflectivity profile at W-band for overpass of Atlantic Hurricane Igor on 16 Sept 2010 between 1713 and 1728 UTC (corresponding to along-track distance of 2200 km). The ECMWF line-of-sight winds projected onto the CloudSat curtain are plotted as arrows. Right panel: Contour plot of ECMWF line-of-sight winds. The reflectivity data are provided at CloudSat resolution (1.1 km horizontal, 0.5 km vertical) whereas the ECMWF winds are at  $0.1^\circ$  resolution ( $\sim 10 \text{ km}$ ). For presentation purposes only winds every 10 km along the curtain and every 700 m in the vertical are shown (left panel).

started weakening. Fig. 3 shows the CloudSat radar vertical reflectivity profile derived from the 2B-GEOPROF product across the whole hurricane: the system extends for about 2200 km horizontally with clouds towering to almost 16 km. Some deep

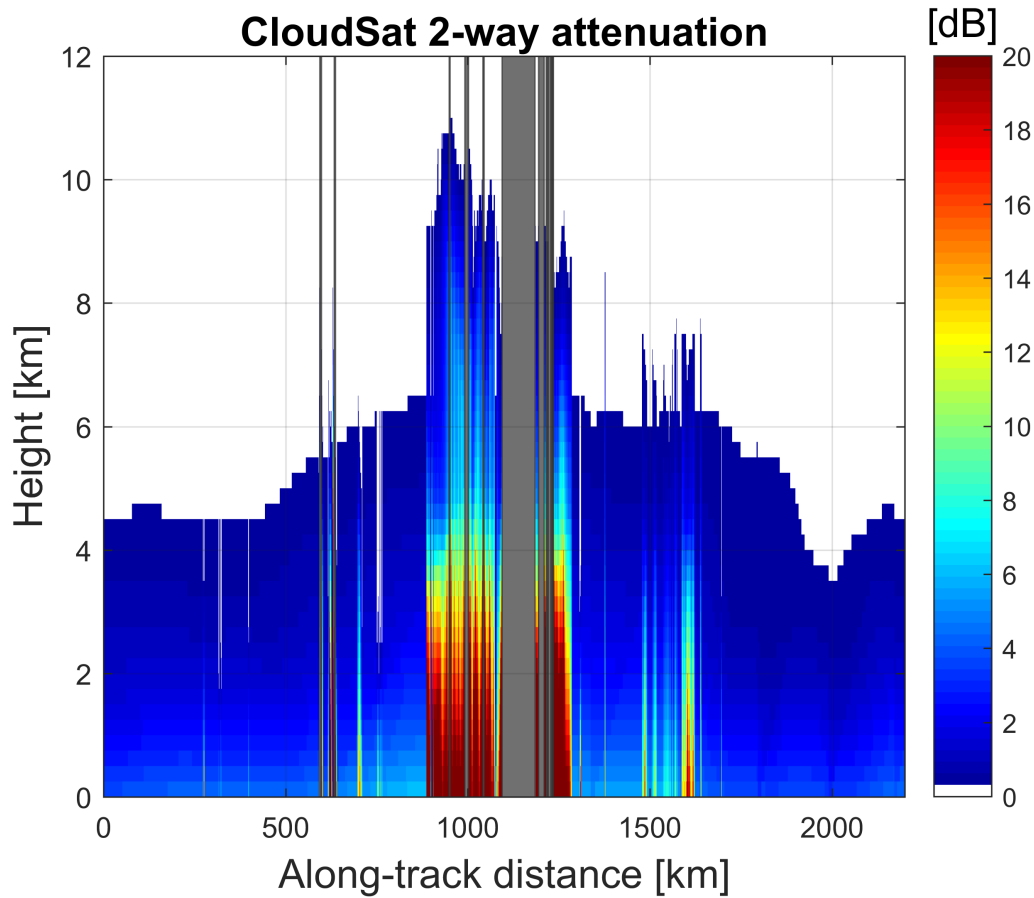


**Figure 4.** Two-way attenuation as retrieved in the 2C-RAIN product for the scene shown in Fig. 3. Grey bands correspond to profiles where the retrieval in the 2C-RAIN product is not applicable. Data are provided at CloudSat resolution (1.1 km horizontal, 0.5 km vertical).

convection and heavy precipitation are clearly present close to the centre of the plot corresponding to the eye wall: attenuation is so strong that even the surface signal is completely attenuated. Some deep isolated convective towers are present to the South (left side of the panel) in association with the spiral bands. The cirrus canopy stretches across most of the overpass, but it is much taller in the Southern part.

- 5 The wind field of course varies appreciably over the scene, and this is exemplified by the characteristic change in the line-of-sight velocity component that occurs across the hurricane (indicated by the arrows in Fig. 3). This line-of-sight component, which is determined by combining ECMWF and CloudSat data, varies significantly over the horizontal extent of the hurricane, with values ranging from approximately  $-10$  to  $+30$   $\text{m s}^{-1}$  at along-track distances of about 0 and 1000 km respectively (Fig. 3). The region with the highest wind magnitudes is associated with the upper levels in the central tallest part of the system.

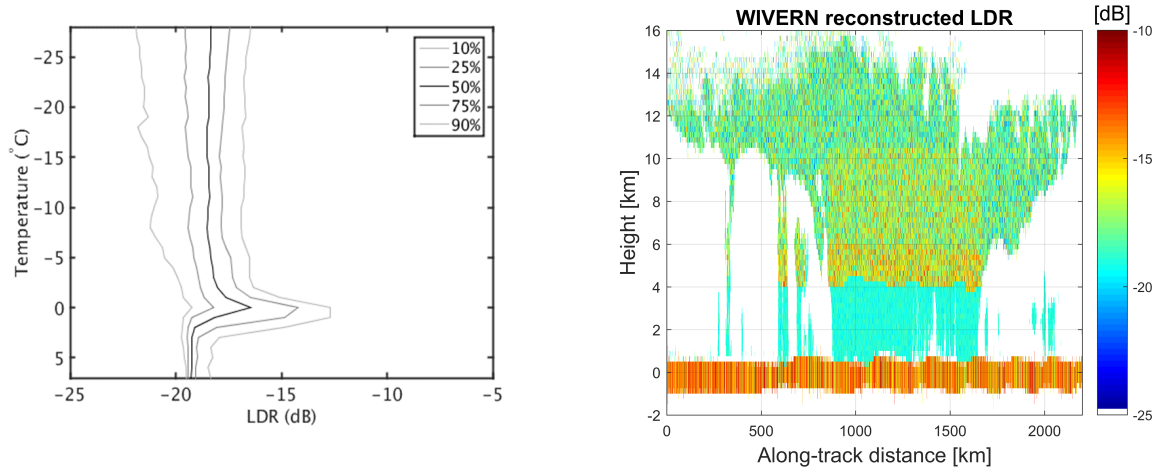


**Figure 5.** Left panel: climatological observations of W-band  $LDR$  at the Chilbolton observatory for an elevation angle of  $45^\circ$  (courtesy of John Nicol, University of Reading). Right panel: simulated  $LDR$  for the scene shown in Fig. 3 at CloudSat resolution (1.1 km horizontal, 0.5 km vertical).

10 The 2C-RAIN product reconstructs vertical profiles of attenuation (see Fig. 4) and of effective reflectivities based on an optimal estimation framework. The retrieval is not applicable in regions of strong convection in the presence of multiple scattering and high attenuation (Matrosov et al., 2008; Battaglia et al., 2011) where no convergence of the algorithm is obtained. These regions are marked by the grey stripes in Fig. 4. No reconstruction of simulated profiles will be attempted in such regions. Note that in regions filled with precipitation the 2-way path-integrated attenuation can exceed 30 dB.

To simulate a Doppler radar with polarization diversity linear depolarization ratio ( $LDR$ ) profiles are also needed (see discussion later in Sect. 3.3.3). A crude  $LDR$  is reconstructed based on climatological observations of  $LDR$  at the Chilbolton observatory (see left panel in Fig. 5). Data were collected during June and July 2017 at  $45^\circ$  elevation with the W-band Galileo polarimetric radar. Different hydrometeors (as derived from the 2B-CLDCLASS-LIDAR product) are assigned  $LDR$  values  
 5 drawn from a normal distribution with 0.5, 1.5, 2 and 1.5 dB standard deviation and mean values of -19, -18, -16 and -17 dB for rain, ice crystals, melting particles and the mixed-phase region, respectively. Surface  $LDR$  are assumed to be normally distributed around -14 dB and -7 dB for sea and land respectively with 2 dB standard deviation (Battaglia et al., 2017).

To produce realistic simulations of slant-looking radars, two aspects must be accounted for.

1. The slant viewing geometry (with an increased cumulative attenuation compared to nadir-looking radar) and the appropriate antenna pattern (Eq. 1) must be accounted for. This is possible because unattenuated reflectivities and attenuation estimates are available from the 2C-RAIN product so that the measured reflectivity (term  $Z_m$  appearing in the integral of Eq. 2) can be properly computed for each direction of the antenna pattern; the integration over the backscattering volume  
 10

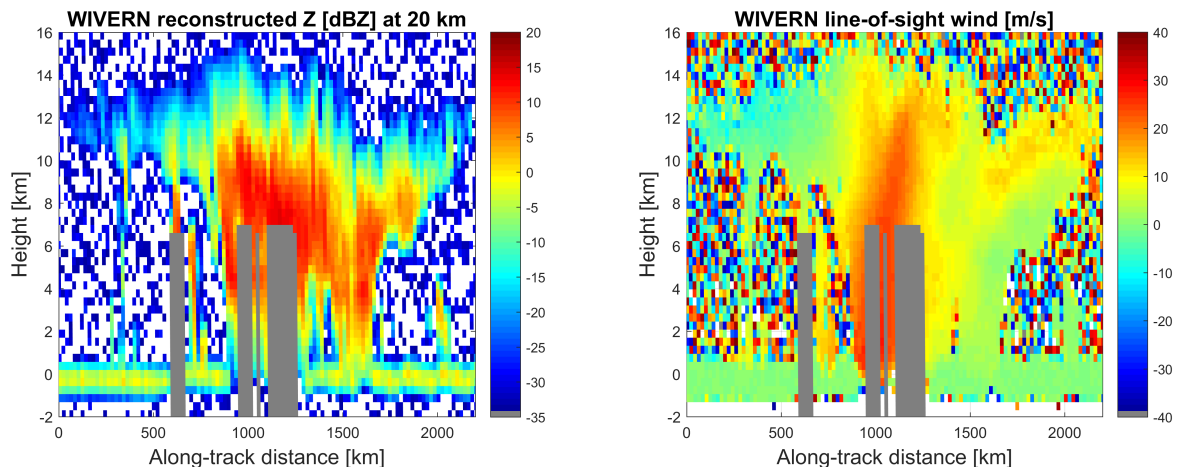


**Figure 6.** Reconstructed reflectivity (left) and line-of-sight Doppler velocities (right) simulated for a system with the specifics listed in Tab. 1 and starting from the CloudSat scene illustrated in Fig. 3. The regions shaded in grey correspond to areas where no reconstruction of the reflectivity profile is possible due to severe attenuation/multiple scattering. Reflectivities and Doppler velocities are produced with a 20 km integration length for a total of 200  $H - V$  pairs with a  $T_{hv} = 20 \mu\text{s}$  (which corresponds to a Nyquist velocity of  $40 \text{ ms}^{-1}$ ).

is carried out at the initial 1.1 km integration length of CloudSat. Further along-track averaging is performed later (e.g. resolution of winds for data assimilation is about 20 km).

2. The ground clutter must be significantly reduced, especially over ocean. In Fig. 3 the ocean surface return is very strong because CloudSat is almost nadir looking. On the other hand, in the configuration shown in Fig. 2, the surface clutter will be significantly lower. Recent airborne studies at 94 GHz and WIVERN incidence angles (Battaglia et al., 2017) have established the natural variability of the normalized radar surface backscattering,  $\sigma_0$ . Accordingly in this study, sea (land) surface  $\sigma_0$  values have been assumed to be normally distributed around -25 dB (-8 dB) with standard deviation equal to 5 dB (4 dB).

The result of the simulator is shown in Fig. 6. Note that the grey stripes correspond to the regions where no attenuation correction is deemed possible, which go from approximately 2 km above the freezing level to the ground corresponding to the grey bands where the 2C-RAIN product is not applicable (grey stripes in Fig. 4). Because of the slant geometry and the 20 km integration the grey bands are now wider than for Fig. 4.

### 3.3 Errors

The simulation framework is ideal for properly assessing Doppler (reflectivity-weighted) line-of-sight velocity estimate ( $\hat{v}_D$ ) errors on a global scale. Here, we will focus our analysis on three different sources of errors, which are related to the spatial

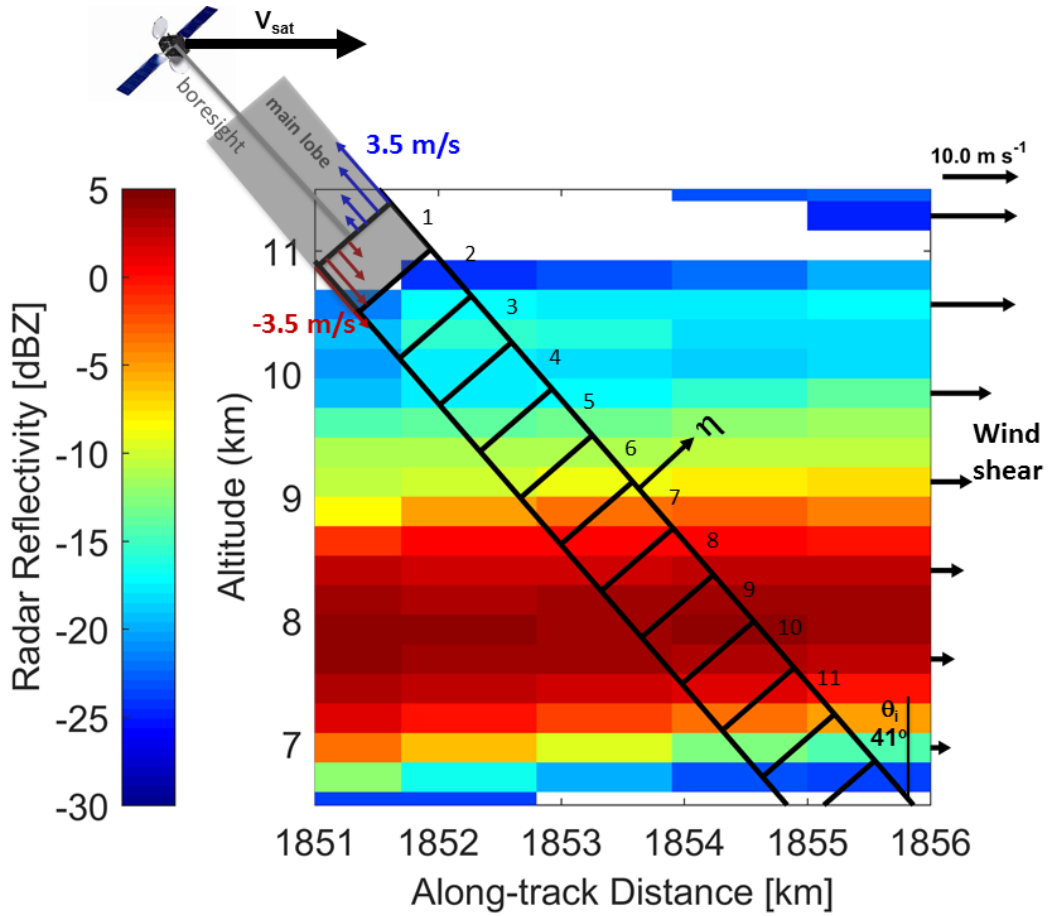


**Figure 7.** Diagram explaining Doppler velocity errors introduced by NUBF. The reflectivity profiles are extracted from hurricane Igor (ice clouds corresponding to the red arrow in the left panel of Fig. 3). The black rectangles represent the backscattering volumes associated with the 3-dB antenna main lobe.

structure of the wind and of the reflectivity fields: errors due to NUBF, to the presence of wind shear and to the cross talk between channels induced by atmospheric targets when adopting polarization diversity.

### 3.3.1 Non uniform beam filling: satellite motion-induced biases

For a fast-moving spaceborne Doppler radar, radar reflectivity gradients within the radar sampling volume can introduce a significant source of error in Doppler velocity estimates (Tanelli et al., 2002). In fact, the component of the satellite velocity along the line of sight presents a shear across the backscattering volume. In Fig. 7 the configuration adopted in Fig. 2 is used to illuminate the small radar volume identified by the red arrow in Fig. 3. If the frequency Doppler shift and the associated Doppler velocity corresponding to the antenna boresight direction are perfectly compensated for and set to zero, then the

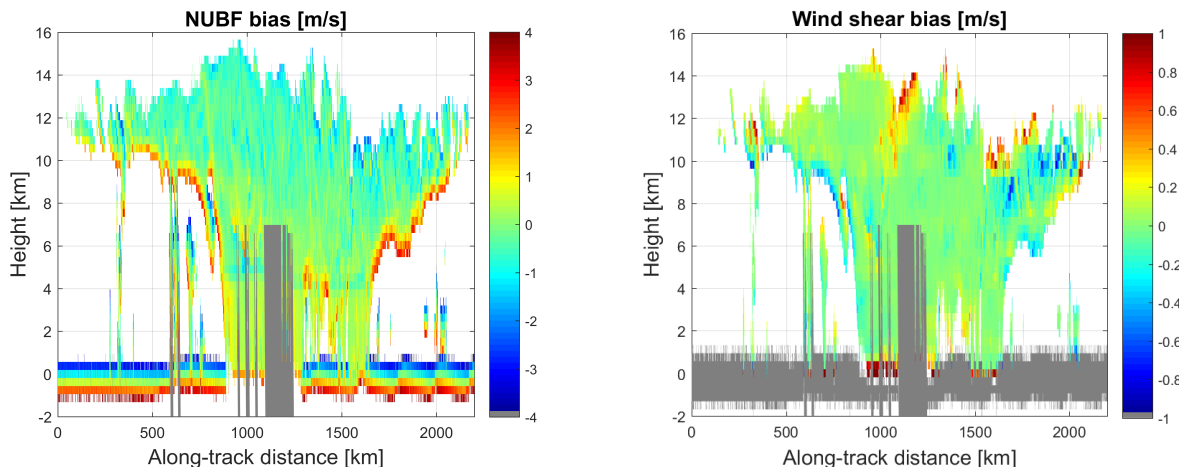


**Figure 8.** NUBF-induced (left panel) and wind-shear-induced (right panel) errors for the hurricane Igor scene shown in Fig. 6. Most of the biases are near the cloud edge; widespread biases of  $\sim 1 \text{ m s}^{-1}$  must be avoided.

forward (backward) part of the backscattering volume appears to move upward (downward) as illustrated by the blue (red) arrows. Across the 3-dB footprint size, this velocity ranges from  $-3.5$  to  $+3.5 \text{ m s}^{-1}$ . When coupled with a reflectivity gradient, this satellite-motion-induced velocity shear can produce a bias. For instance, for the backscattering volumes labelled as 11 (6) in Fig. 7, there is a positive (negative) reflectivity vertical gradient which will produce an upward (downward) bias.

The combined CloudSat and ECMWF datasets have been exploited to quantify the effect of NUBF biases as experienced by a satellite orbiting in a polar sunsynchronous orbit. An estimate of these biases is obtained by considering the difference between  $\hat{v}_D[v_{sat} = 7600 \text{ m s}^{-1}]$  corrected for satellite motion and  $\hat{v}_D[v_{sat} = 0]$  where the satellite velocity is set to  $0 \text{ m s}^{-1}$ . The NUBF-induced bias corresponding to the scene of hurricane Igor depicted in Fig. 6 is shown in Fig. 8. The main feature is represented by upward biases at the cloud top and downward biases at the cloud base, both up to several  $\text{m s}^{-1}$ .

For nadir pointing radars, notional studies demonstrated that such biases can be mitigated by estimating the along-track reflectivity gradient because NUBF-induced biases are expected to be linearly proportional to such reflectivity gradients (Schutgens, 2008; Kollias et al., 2014; Sy et al., 2013). Similarly, in a slant-looking geometry the relevant gradients are those along the direction orthogonal to the boresight and lying in the plane containing the satellite velocity and the antenna boresight direction ( $\eta$  direction in Fig. 7, Battaglia and Kollias (2014a)). If conically scanning systems are considered it will be more challenging to retrieve the Z-gradients along such directions for all scanning angles; moreover it is expected that such gradients will be affected by the vertical reflectivity gradients, which are typically larger than horizontal gradients. In the presence of a vertical reflectivity gradient,  $\nabla_z Z$  (in  $\text{dB m}^{-1}$ ), if the reflectivity field can be approximated to vary linearly within the backscattering volume, then the bias introduced by the satellite motion is equal to (Sy et al., 2013; Battaglia and Kollias, 2014a):

$$\Delta_{satellite\ motion} = v_{sat} \frac{\nabla_z Z r \sin(2\theta_i)}{4.343 \cdot 32 \log(2)} \theta_{3dB}^2 \quad (3)$$

where  $r$  is the range from the radar. For instance, for the “WIVERN” configuration (Tab. 1) this corresponds to a bias of  $0.077 \text{ m s}^{-1}$  per  $\text{dB km}^{-1}$ .

### 3.3.2 Wind shear

Similarly biases in the radar-derived winds may arise when there is a vertical wind shear (see arrows on the right hand side of Fig. 7) coupled with a large vertical gradient of radar reflectivity across the radar backscattering volume. An estimate of these biases is obtained by considering the difference between  $\hat{v}_D$  and  $\hat{v}_{AW}$  where the latter is the line-of-sight velocity estimate averaged over the antenna pattern but not reflectivity-weighted, i.e.

$$v_{AW}(r) = \frac{\iiint_V v_r G^2 dV}{\iiint_V G^2 dV}.$$

For the Hurricane Igor case study, the results are shown in the right panel of Fig. 8: wind-shear-induced biases are generally smaller than NUBF-induced biases with amplitudes up to  $1 \text{ m s}^{-1}$  and confined to the areas at the edge of clouds characterized by large wind shear and vertical reflectivity gradients.

Since the vertical wind shear is generally considerably larger than the horizontal one, under the assumption that the reflectivity and wind fields can be approximated to vary linearly within the backscattering volume, the bias due to wind shear can be approximated as:

$$\Delta_{wind\ shear} = v_D - v_{AW} = \frac{\nabla_z Z \nabla_z v}{4.343} \left[ \frac{\Delta r^2}{12} \cos^2 \theta_i + \frac{r^2 \theta_{3dB}^2}{16 \log(2)} \sin^2 \theta_i \right] \quad (4)$$

where  $\nabla_z Z$  and  $\nabla_z v$  are the reflectivity and wind vertical gradients expressed in  $\text{dB m}^{-1}$  and in  $\text{s}^{-1}$ . For instance for the “WIVERN” configuration (Tab. 1) this corresponds to a bias of  $0.37 \text{ m s}^{-1}$  per  $\text{dB km}^{-1}$  for a wind shear of  $0.01 \text{ s}^{-1}$ . The reflectivity gradients and wind shear along the vertical direction can be inferred from adjacent gates and therefore a correction can be attempted.

### 3.3.3 Cross-talk

Doppler systems adopting polarization diversity assume that the  $V$  and  $H$  waves propagate and scatter independently without any interference. In reality the effect of cross-polarization is to produce an interference signal in each co-polar channel depending on the temporal shift between the  $H$  and  $V$  pair and the strength of the cross-polar power, and appear as “ghost echoes”. Cross-talk between the two polarizations can occur either at the hardware level or can be induced by propagation and/or backscattering in the atmosphere. While the former is typically reduced to values lower than  $-25 \text{ dB}$ , the latter can be important and is characterized by the  $LDR$ . The phases of ghost echoes are incoherent with respect to the echoes of interest so do not bias the velocity estimates, but increase their random error as a function of the signal-to-ghost ratio (Pazmany et al., 1999; Wolde et al., 2018). This quantity depends on the reflectivity profile structure and on  $T_{hv}$ , the time separation between the  $H$ - and  $V$ - polarized pulses. The full theory is reviewed in depth in Wolde et al. (2018), formulas (6-11). An example of the line-of-sight measured Doppler velocity for a  $T_{hv} = 20 \mu\text{s}$  is shown in the right panel of Fig. 6 for the “WIVERN forward”

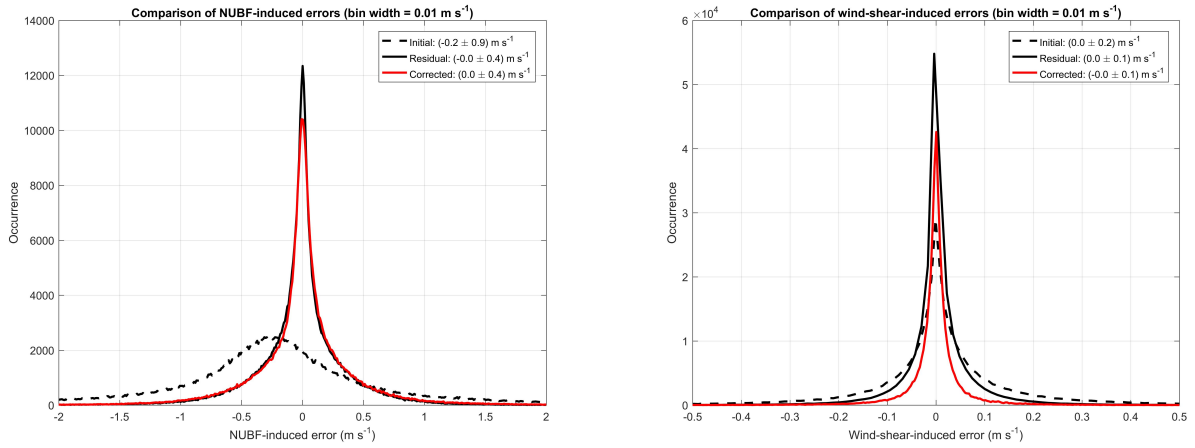


**Figure 9.** Left (right) panel: distribution of 8-day CloudSat dataset NUBF-induced (wind-shear-induced) errors. Black dashed line: initial errors; black solid line: errors after correction with perfect measurements; red line: errors after correction with noisy measurements. A  $T_{hv} = 20 \mu\text{s}$  and a spectral Doppler width of  $4 \text{ m s}^{-1}$  have been assumed when including noise.

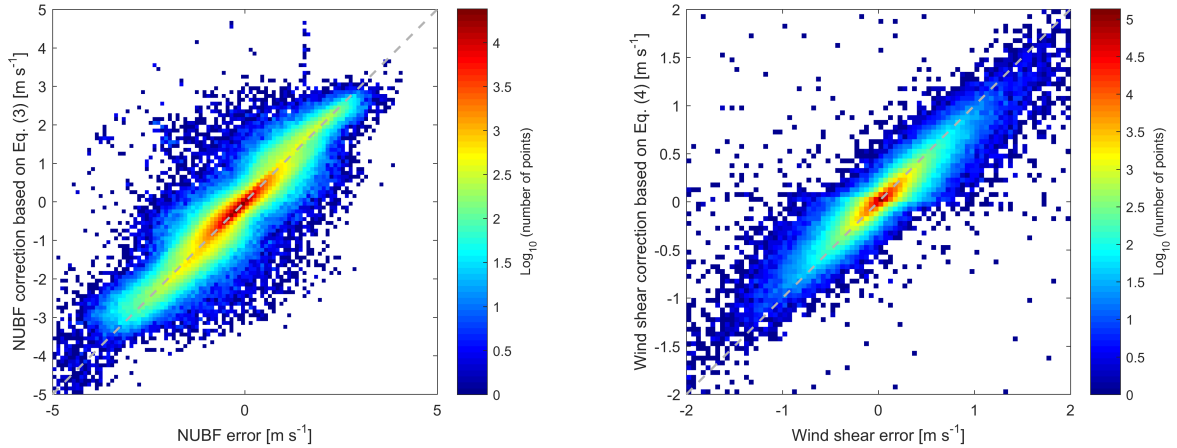


**Figure 10.** Left (right) panel: density plot for the 8-day CloudSat dataset illustrating the NUBF-induced (wind-shear-induced) bias vs bias correction estimated according to Eq. 3 (Eq. 4).

configuration. The Doppler winds compare well with those from ECMWF, shown in the right panel of Fig. 3. Note how the measurements become increasingly noisier when moving towards lower SNRs.

## 4 Statistical analysis

Eight days of CloudSat data, from 1 to 8 Sept 2010, have been used to obtain simulated residual errors, defined as the difference between the actual velocity biases and the velocity corrections obtained using the formulae given above. The dataset comprises 94 granules and therefore covers a variety of cloud types with a multitude of characteristics. The CloudSat data granules used for this study were chosen based upon whether data files corresponding to the four relevant CloudSat data products (2B-GEOPROF, 2B-CLDCLASS, 2C-RAIN-PROFILE and ECMWF-AUX) were all present simultaneously.

### 4.1 NUBF and wind shear errors and corrections

The technique demonstrated for Hurricane Igor in Sect. 3.2 has been applied to the whole dataset. First the magnitudes of the errors induced by NUBF and wind shear are evaluated, e.g. the wind-shear-induced biases are obtained by subtracting the ECMWF (antenna-weighted) winds from the reflectivity-weighted winds. The black dashed lines in Fig. 9 show the distribution for the NUBF-induced (left) and wind-shear-induced error (right), with the former significantly larger (standard deviation of  $0.9 \text{ m s}^{-1}$  vs  $0.2 \text{ m s}^{-1}$ ) compared to the latter and slightly biased ( $-0.30 \text{ m s}^{-1}$ ). This bias is due to the fact that the average reflectivity vertical gradient (when all heights are considered) is slightly negative. Note that this bias will cancel out if a backward look is also adopted (as for the conically scanning WIVERN).

Since CloudSat reflectivity and ECMWF wind fields are defined at coarse horizontal scales the simulation may not account for the full variability inside the backscattering volume; thus the errors may be underestimated. Second, the quality of the corrections derived from the formulae given by Eqs. (3-4) is tested by comparing NUBF-induced and wind-shear-induced errors with their corresponding corrections (left and right panels of Fig. 10, respectively, which are occurrence density plots with the colours corresponding to  $\log_{10} N$ , where  $N$  is the number of points in the bin). So far, the reflectivity and Doppler velocity measurements have been assumed to be free of noise. Clearly the corrections to NUBF- and wind-shear-induced errors appear to match very well the actual NUBF- and wind-shear-induced biases. This implies that a very accurate wind field can be constructed from the reflectivity-weighted winds with standard deviations reduced to  $0.4$  and  $0.1 \text{ m s}^{-1}$  (see solid black lines in Fig. 9).

However real reflectivity and Doppler velocity data are subject to noise, whose impact will depend upon the SNR value. In the selected configuration a single-pulse SNR of  $0 \text{ dB}$  corresponds to an echo of  $-19 \text{ dBZ}$ . For instance, in terms of velocity errors, for a  $20 \text{ km}$  along track integration (i.e.  $200$  pulse pairs) the errors due to the pulse pair processing are of the order of  $1.5 \text{ m s}^{-1}$  at  $0 \text{ SNR}$  (see Fig. 3 in Illingworth et al. (2018b)).

In order to ascertain whether accurate wind fields can be retrieved from the Doppler radar data, it is necessary to examine how well the vertical reflectivity and Doppler velocity gradients, which enter Eqs. (3-4), can be obtained in the presence of varying levels of noise. The effectiveness of the wind corrections therefore has been studied by injecting noise into the reflectivities and Doppler velocity fields. This noise has been assumed to take the form of normally distributed fluctuations whose magnitudes are determined by the actual SNR, the spectral width of the Doppler spectrum and the selected  $T_{hv}$  (according to formula 6 in Hogan et al. (2004) for the reflectivity noise and formula 15 in Pazmany et al. (1999) for the Doppler velocity noise). Since the

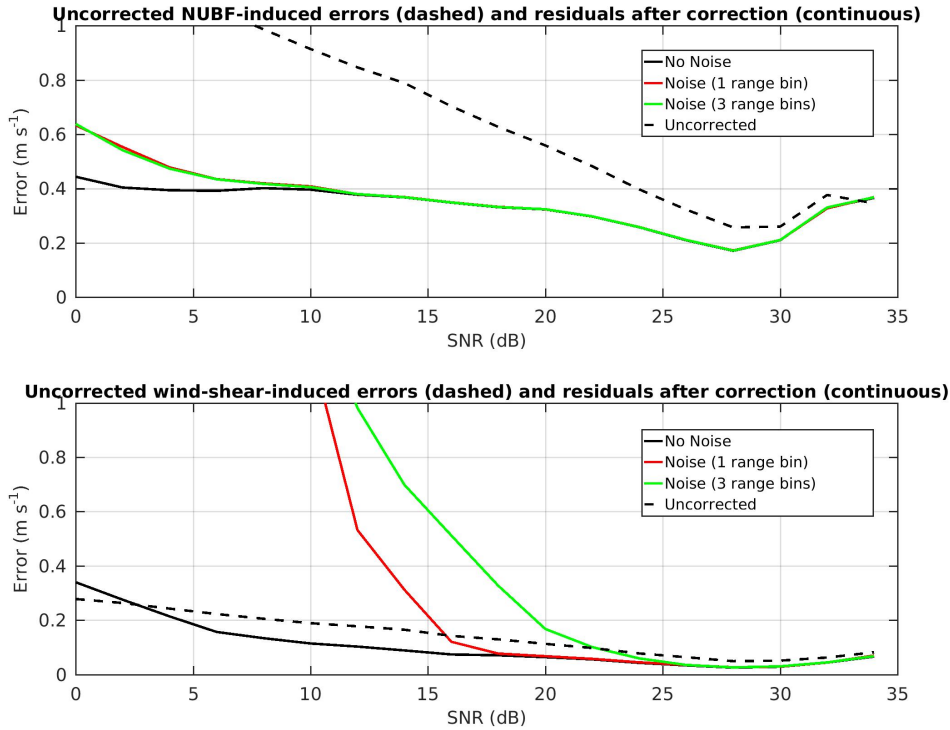


**Figure 11.** The NUBF-induced (top) and wind-shear-induced (bottom) root-mean-square errors as a function of the SNR computed: 1) without noise (black solid lines); 2) with added noise and estimating gradients from variables at the native range resolution of 500 m (red solid lines); 3) with added noise and estimating gradients from variables computed from running averages over three range bins (green solid lines). The statistics is built from eight days of CloudSat data. Initial uncorrected errors are plotted as black dashed lines.

addition of noise causes large variations in reflectivity and wind gradients obtained from noisy data, efforts have been made to mitigate any consequent negative effects by applying a running mean to the data along the line of sight (averaging over three range bins) with the intent of smoothing them before the gradients are computed. The solid red lines in Fig. 9 show the distribution of the errors associated to NUBF (left) and wind shear (right) once the corrections described by formulas (3-4) are applied based on velocity and reflectivity gradients estimated after the injection of noise into reflectivities and Doppler velocities. No range averaging is performed. Note that the wind-shear-induced correction (right panel) is applied only for  $SNR \geq 16$  dB (see discussion here below).

The errors in the wind estimates due to the NUBF-induced and wind-shear-induced effects are shown in Fig. 11 (top and bottom panels, respectively) as a function of the SNR. The horizontal axis shows the signal-to-noise ratio, with 0 dB corresponding to a reflectivity of -19 dBZ, and the vertical axis shows the root mean square errors (RMSE) computed with reference to the

“true wind” (i.e. the one that would be measured without reflectivity gradients). The initial RMSEs where the corrections given  
30 by Eq.3 and Eq.4 have not been applied are shown as black dashed lines. The RMSEs are recalculated after the corrections are applied. Three conditions are examined. The corrections are applied: 1) without adding any noise to the measurements (black solid line); 2) by adding noise to the measurements as expected for the WIVERN system (red solid lines); 3) by adding noise and estimating gradients after applying running averages over three range bins of  $\sim 0.5$  km (green solid lines).

Clearly the corrections for NUBF-induced RMSEs vary little with SNR. Even without range averaging, the correction based on Eq. (3) produces results similar to those for the perfect correction without any noise (black solid line), and is only slightly worse for  $SNR < 10$  dB. It is worth applying the correction as the RMSEs are reduced significantly from their initial value (black dashed line). There is an increase in the NUBF-induced RMSEs for SNR above about 28 dB, although the error remains below  $0.4 \text{ m s}^{-1}$ . This is caused by a tendency for data to deviate away from the one-to-one line (grey dashed line in Fig. 10) at the highest SNR values, thus suggesting that at higher reflectivities the correction becomes less linear. As a result, the correction given by Eq. 3 may be less effective at these highest SNR values. Horanyi et al. (2014) show that the bias must be less than  $1 \text{ m s}^{-1}$  but that higher random errors are acceptable: the errors here documented appear to largely fulfill such conditions.

For the case of wind-shear-induced RMSEs, the correction clearly becomes more effective only at high SNR in presence of  
5 noise, with the RMSEs computed in such condition approaching those computed without noise only for  $SNR \sim 20$  dB (red vs black line). For  $SNR < 20$  dB, there is a significant deviation between the noise and no-noise cases. The initial wind-shear-induced error computed without any correction (dashed line) is very small for all SNR. While the correction would further reduce the RMSE in presence of perfect measurements with no noise (black line), the contrary is true in presence of noise for all values of  $SNR < 20$  dB (red solid vs black dashed line). This increase in the wind-shear-induced RMSE is caused  
10 by noise-induced variations in the velocity gradient. These noise-induced changes render the correction ineffective at lower SNR. Interestingly, averaging over three vertical range bins makes the correction worse (green solid line) with the corrected value only approaching the no-noise value at about 25 dB SNR. In contrast to the case for NUBF-induced errors, where the correction produces notable improvement for all SNR values, the correction for wind-shear-induced effects will reduce the error significantly only if it is applied for  $SNR > 18$  dB.

## 15 4.2 Cross-talk errors and optimal $T_{hv}$ selection

Simulations of Doppler velocities have been generated using  $T_{hv}$  values ranging from 5 to 40  $\mu\text{s}$ , taking into account the SNR and the strengths of the ghost echoes for 20-km along-track integration. The fraction of profiles for which a “WIVERN forward” configuration is expected to produce winds with accuracy better than  $2 \text{ m s}^{-1}$  is presented in Fig. 12 for high-latitudes (top), mid-latitudes (middle) and tropical (bottom panel) oceanic conditions. Dashed (continuous) lines correspond to results  
20 when the ghosts are (are not) accounted for. Clearly, the ghosts only marginally reduce the number of WIVERN measurements with accuracy better than  $2 \text{ m s}^{-1}$ . Specifically, the number of measurements with good accuracy is reduced by 1.8%, 0.9% and 0.3% for  $T_{hv}$  of 5, 20 and 40  $\mu\text{s}$  respectively.

The fraction is much lower for the 5  $\mu\text{s}$   $T_{hv}$  values because at this pair separation a small noise in the phase maps into a large velocity error. Overall, Fig. 12 shows that in the mid-troposphere (3-8 km) “WIVERN forward” would provide a useful

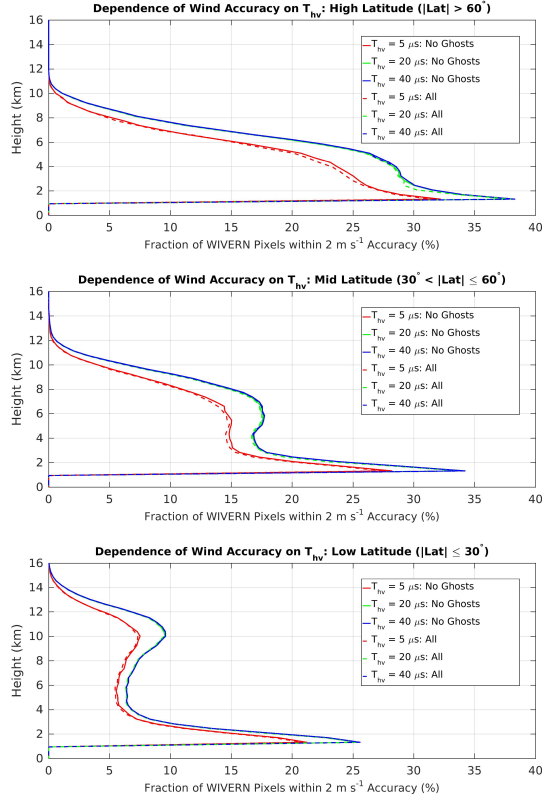


**Figure 12.** The fraction of profiles (including cloudy and non-cloudy situations) where winds at a given height can be derived with an accuracy of  $2 \text{ m s}^{-1}$  for various  $T_{hv}$  values for high-latitudes (top), mid-latitudes (middle) and tropical (bottom panel) oceanic conditions. Dashed (continuous) lines correspond to results when the ghosts are (are not) accounted for. A “WIVERN forward” configuration has been assumed (see Tab. 1) with an along-track integration length of 20 km. The WIVERN profiles have been reconstructed from CloudSat profiles over ocean with  $LDR$  and clutter signals reconstructed based on airborne observations of ocean surface returns.

25 measurement 10% of the observation time, but this is expected to be significantly reduced over land at heights around 2 and around 4 km where the bright land surfaces produce ghost echoes for  $T_{hv}$  of 20 and 40  $\mu\text{s}$ , respectively.

The selection of an optimal  $T_{hv}$  certainly accounts for the result produced in Fig. 12 but other factors must also be considered:

1. Aliasing must be avoided. A  $T_{hv} = 20 \mu\text{s}$  corresponding to a Nyquist velocity  $v_N \sim 40 \text{ m s}^{-1}$  is certainly advantageous compared to a  $T_{hv} = 40 \mu\text{s}$  corresponding to a  $v_N \sim 20 \text{ m s}^{-1}$  when winds in extreme weather events are sought after.

- 30 2. Winds in the mid-troposphere are considered to be more important than winds in the lower troposphere. This is because there is a lack of winds in the middle troposphere (see Fig. 9 in Illingworth et al. (2018b)) and because winds in the lower troposphere are more affected by boundary layer dynamics (which are less long-lived and therefore more difficult to assimilate). As a result it is preferable to have the surface ghosts as close to the surface as possible. Here only sea surfaces have been considered; land surfaces are much brighter (Battaglia et al., 2017) and therefore surface ghosts will play a more notable role. Again, this favours smaller  $T_{hv}$ , e.g.  $T_{hv} = 20 \mu\text{s}$  (ghost layer centred at 2.2 km) vs  $40 \mu\text{s}$  (ghost layer centred at 4.5 km).
- 5 3. In the presence of large turbulence the Doppler spectral width can increase and greatly exceed the value predicted by accounting for the satellite motion only (Battaglia and Kollias, 2014a). This decreases the coherency time of the medium and, as a consequence, the optimal  $T_{hv}$  value that minimizes the noise error is also reduced (see Fig. 8 in Battaglia and Kollias (2014a)).

## 5 Conclusions and future work

CloudSat observations and Level 2 products have been used in combination with collocated ECMWF wind reanalysis to simulate spaceborne oblique-viewing W-band Doppler observations for radars adopting polarization diversity, which have been recently proposed within the Earth Observation programmes of various space agencies. A specific radar configuration (the “WIVERN”, see Tab. 1), recently proposed for the ESA-Earth Explorer 10 call, is analysed in detail in this study. The simulator capitalizes on the fact that the CloudSat W-band Cloud Profiling Radar is in a polar orbit and therefore provides realistic global patterns of the radar reflectivity spatial variability at the W-band frequency range (and, when combined with ECMWF-winds, of how such patterns co-vary with the wind-field), which are key drivers for establishing the performance of a W-band Doppler system on the global scale. The simulator is particularly suited for assessing the relevance of non-uniform beam filling and wind-shear driven errors and of the effectiveness of their corrections based on the estimates of vertical gradients of the reflectivity and wind fields.

For data assimilation, properly quantified random wind errors are generally acceptable but biases larger than  $1 \text{ m s}^{-1}$  cannot be tolerated. Our testing dataset based on roughly 100 CloudSat granules shows that for an instrument looking at  $41^\circ$  slant angle and for a 20 km integration, both wind shear and NUBF introduce almost unbiased errors (biases of  $-0.3$  and  $0 \text{ m s}^{-1}$ , respectively) with standard deviations of the order of  $0.9$  and  $0.2 \text{ m s}^{-1}$ . Such errors can be reduced if vertical gradients of reflectivity and of the wind can be estimated via Eqs. (3-4). If vertical gradients are perfectly estimated then the residuals in the Doppler velocities are unbiased and their standard deviations can be reduced to  $0.2$  and  $0.1 \text{ m s}^{-1}$ . Practically, the corrections for both NUBF-induced and wind-shear-induced errors are effective in producing unbiased velocities (and perform at their best with  $\text{SNR} > 10 \text{ dB}$  and  $\text{SNR} > 20 \text{ dB}$  respectively).

The simulator also allows the quantification of the average number of accurate measurements that could be potentially gathered by the Doppler radar for each orbit. This is strongly impacted by the selection of the polarization diversity  $H - V$  pulse separation,  $T_{hv}$ . For the WIVERN slant configuration a selection close to  $20 \mu\text{s}$  seems to achieve the right balance

between maximizing the number of accurate wind measurements (exceeding 10% in the mid-troposphere), and minimizing  
20 aliasing effects in the presence of high winds. The presence of cross-talk reduces only marginally the region of measurements  
with good accuracy.

This study represents the first step towards a more sophisticated development of end-to-end simulators for spaceborne  
oblique viewing Doppler radars adopting polarization diversity. Further work could improve the simulator along the following  
guidelines.

- 25 1. The CloudSat radar only provides a 2D curtain, and thus does not capture the full 3D structure of clouds. Moreover its  
vertical (500 m) and horizontal ( $1.4 \times 1.7 \text{ km}^2$ ) resolutions (Stephens et al., 2008) are not optimal for fully characterizing  
the spatial variability within the scattering volumes envisaged for future spaceborne W-band Doppler radars. Future  
scanning radar missions will be able to provide 3D structure of clouds (e.g. Durden et al. (2016)), and are expected to be  
30 launched in the next decade (The Decadal Survey, 2017). In the meantime, cloud down-scaling algorithms and stochastic  
models such as those proposed in e.g. Venema et al. (2010); Barker et al. (2011) could be applied to the CloudSat dataset  
in order to mimic the natural variability at smaller scales.
2. The effective reflectivity is retrieved for CloudSat profiles only over ocean, where an estimate of the path-integrated  
attenuation is possible via the surface reference technique (Haynes et al., 2009). The analysis conducted in this paper is  
therefore limited to ocean cases only. The EarthCARE Cloud Profiling Radar, expected for launch in 2020 (Illingworth  
et al., 2015), with the inclusion of Doppler capabilities has the potential to enable estimates of rain rate without the  
need for an estimate of the path-integrated attenuation (Mason et al., 2017). Therefore the reconstruction of effective  
reflectivity and attenuation profiles should become possible over land as well.
3. The ECMWF wind fields are defined at coarse horizontal scales whereas the effective vertical resolution exceeds 1.5 km  
5 so that they generally tend to underestimate the vertical wind shear (Houchi et al., 2010), with mean and median values  
of wind shears from radiosondes a factor of two larger than ECMWF outputs. Reanalysis at finer resolutions like ERA-5  
should mitigate this issue.

*Acknowledgements.* This work was supported in part by the European Space Agency under the activity Doppler Wind Radar Demonstrator  
(ESA-ESTEC) under Contract 4000114108/15/NL/MP and in part by CEOI-UKSA under Contract RP10G0327E13. The work by Alessandro  
10 Battaglia has been supported by the project Radiation and Rainfall funded by the UK National Center for Earth Observation. This research  
used the ALICE High Performance Computing Facility at the University of Leicester.

## References

- Barker, H. W., M. Jerg, T. Wehr, S. Kato, D. Donovan, and R. Hogan, 2011: A 3D cloud-construction algorithm for the EarthCARE satellite mission. *Quart. J. Roy. Meteor. Soc.*, **137**, 1042–1058, doi:10.1002/qj.824.
- Battaglia, A., T. Augustynek, S. Tanelli, and P. Kollias, 2011: Multiple scattering identification in spaceborne W-band radar measurements of deep convective cores. *J. Geophys. Res.*, **116 (D19201)**, doi:10.1029/2011JD016142.
- 5 Battaglia, A. and P. Kollias, 2014a: Error Analysis of a Conceptual Cloud Doppler Stereoradar with Polarization Diversity for Better Understanding Space Applications. *J. Atmos. Ocean Technol.*, **32 (7)**, 1298–1319, doi: <http://dx.doi.org/10.1175/JTECH-D-14-00015.1>.
- Battaglia, A. and P. Kollias, 2014b: Using ice clouds for mitigating the EarthCARE Doppler radar mispointing. *IEEE Trans. Geosci. Remote Sens.*, **53 (4)**, doi: 10.1109/TGRS.2014.2353219.
- Battaglia, A. and S. Tanelli, 2011: DOppler MULTiple Scattering simulator. *IEEE Trans. Geosci. Remote Sens.*, **49 (1)**, 442–450, doi:10.1109/TGRS.2010.2052818.
- 10 Battaglia, A., S. Tanelli, and P. Kollias, 2013: Polarization diversity for millimeter space-borne Doppler radars: an answer for observing deep convection? *J. Atmos. Ocean Technol.*, **30 (12)**, 2768–2787, doi: <http://dx.doi.org/10.1175/JTECH-D-13-00085.1>.
- Battaglia, A., M. Wolde, L. P. D’Adderio, C. Nguyen, F. Fois, A. Illingworth, and R. Midthassel, 2017: Characterization of Surface Radar Cross Sections at W-Band at Moderate Incidence Angles. *IEEE Trans. Geosci. Remote Sens.*, **55 (7)**, 3846–3859, doi:10.1109/TGRS.2017.2682423.
- 15 Bony, S., B. Stevens, D. M. W. Frierson, C. Jakob, M. Kageyama, R. Pincus, and M. Webb, 2015: How well do we understand and evaluate climate change feedback processes? *Nature Geoscience*, **8 (4)**, 261–268, doi:10.1038/ngeo2398.
- Burns, D., P. Kollias, A. Tatarevic, A. Battaglia, and S. Tanelli, 2016: The Performance of the EarthCARE Cloud Profiling Radar in Marine Stratiform Clouds. *J. Geophys. Res. Atm.*, **14**, 14,525–14,537, doi:10.1002/2016JD025090.
- 20 Doviak, R. J. and D. S. Zrnić, 1993: *Doppler Radar and Weather Observations*. Academic Press.
- Durden, S. L., S. Tanelli, L. W. Epp, V. Jamnejad, E. M. Long, R. M. Perez, and A. Prata, 2016: System design and subsystem technology for a future spaceborne cloud radar. *IEEE Geosci. Remote Sens. Lett.*, **13 (4)**, 560–564.
- Haynes, J. M., T. L’Ecuyer, G. L. Stephens, S. D. Miller, C. Mitrescu, N. B. Wood, and S. Tanelli, 2009: Rainfall retrieval over the ocean with spaceborne W-band radar. *J. Geophys. Res.*, **114 (D00A22)**, doi:10.1029/2008JD009973.
- 25 Hogan, R. J., M. D. Behera, E. J. O’Connor, and A. J. Illingworth, 2004: Estimate of the global distribution of stratiform supercooled liquid water clouds using the LITE lidar. *Geophys. Res. Lett.*, **31 (L05106)**, doi:10.1029/2003GL018977.
- Hogan, R. J., M. P. Mittermaier, and A. J. Illingworth, 2006: The retrieval of ice water content from radar reflectivity factor and temperature and its use in the evaluation of a mesoscale model. *J. Appl. Meteorol.*, **45**, 301–317.
- Horanyi, A., C. Cardinali, M. Rennie, and L. Isaksen, 2014: The assimilation of horizontal line-of-sight wind information into the ECMWF data assimilation and forecasting system. Part I: The assessment of wind impact. *Quart. J. Roy. Meteor. Soc.*, **141**, 1223–1232, <http://dx.doi.org/10.1002/qj.2430>.
- 30 Houchi, K., A. Stoffelen, G. J. Marseille, and J. D. Kloe, 2010: Comparison of wind and wind shear climatologies derived from high-resolution radiosondes and the ECMWF model. *J. Geophys. Res.*, **115 (D22123)**, doi:10.1029/2009JD013196.
- Illingworth, A. J., et al., 2015: The EarthCARE Satellite: the next step forward in global measurements of clouds, aerosols, precipitation and radiation. *Bull. Amer. Met. Soc.*, doi: <http://dx.doi.org/10.1175/BAMS-D-12-00227.1>.
- 35

- Illingworth, A. J., et al., 2018a: Wivern: A new satellite concept to provide global in-cloud winds, precipitation and cloud properties. *Bull. Amer. Met. Soc.*, doi: 10.1175/BAMS-D-16-0047.1, in press.
- Illingworth, A. J., et al., 2018b: WIVERN (WInd VELOCITY RADAR Nephoscope). Proposal submitted to ESA in response to the Call for Earth Explorer-10 Mission Ideas.
- Kollias, P., S. Tanelli, A. Battaglia, and A. Tatarevic, 2014: Evaluation of EarthCARE Cloud Profiling Radar Doppler Velocity Measurements in Particle Sedimentation Regimes. *J. Atmos. Ocean Technol.*, **31**, 366–386, doi: <http://dx.doi.org/10.1175/JTECH-D-11-00202.1>.
- Leinonen, J., M. D. Lebsock, S. Tanelli, K. Suzuki, H. Yashiro, and Y. Miyamoto, 2015: Performance assessment of a triple-frequency spaceborne cloud-precipitation radar concept using a global cloud-resolving model. *Atm. Meas. Tech.*, **8**, 3493–3517, doi:10.5194/amt-8-3493-2015.
- Mace, G. G., R. Marchand, Q. Zhang, and G. Stephens, 2007: Global hydrometeor occurrence as observed by CloudSat: Initial observations from summer 2006. *Geophys. Res. Lett.*, **34**, L09808, doi:10.1029/2006GL029017.
- Mason, S. L., J. C. Chiu, R. J. Hogan, and L. Tian, 2017: Improved rain rate and drop size retrievals from airborne Doppler radar. *Atmos. Chem. Phys.*, **17**, 11 567–11 589, doi.org/10.5194/acp-17-11567-2017.
- Matrosov, S. Y., A. Battaglia, and P. Rodriguez, 2008: Effects of Multiple Scattering on Attenuation-Based Retrievals of Stratiform Rainfall from CloudSat. *J. Atmos. Ocean Technol.*, **25** (12), 2199–2208, doi: 10.1175/2008JTECHA1095.1.
- McNally, A. P., 2002: A note on the occurrence of cloud in meteorologically sensitive areas and the implications for advanced infrared sounders. *Quart. J. Roy. Meteor. Soc.*, **128**, 2551–2556.
- Pazmany, A., J. Galloway, J. Mead, I. Popstefanija, R. McIntosh, and H. Bluestein, 1999: Polarization Diversity Pulse-Pair Technique for Millimetre-Wave Doppler Radar Measurements of Severe Storm Features. *J. Atmos. Ocean Technol.*, **16**, 1900–1910.
- Sassen, K., Z. Wang, and D. Liu, 2008: The global distribution of cirrus clouds from CloudSat/CALIPSO measurements. *Geophys. Res. Lett.*, **113** (D00A12), doi:10.1029/2008JD009972.
- Schutgens, N. A. J., 2008: Simulated Doppler Radar Observations of Inhomogeneous Clouds: Application to the EarthCARE Space Mission. *J. Atmos. Ocean Technol.*, **25** (9), 1514–1528, doi: 10.1175/2007JTECHA1026.1.
- Stephens, G. L., et al., 2008: CloudSat mission: Performance and early science after the first year of operation. *J. Geophys. Res.*, **113**, D00A18, doi: 10.1029/2008JD009982.
- Stoffelen, A., et al., 2005: The Atmospheric Dynamics Mission for Global Wind Field Measurement. *Bull. Amer. Met. Soc.*, **86**, 73–87.
- Sy, O., S. Tanelli, P. Kollias, and Y. Ohno, 2014: Application of Matched Statistical Filters for EarthCARE Cloud Doppler Products. *IEEE Trans. Geosci. Remote Sens.*, **52** (11), 7297–7316.
- Sy, O., S. Tanelli, N. Takahashi, Y. Ohno, H. Horie, and P. Kollias, 2013: Simulation of EarthCARE Spaceborne Doppler Radar Products using ground-based and airborne data: effects of aliasing and non-uniform beam filling. *IEEE Trans. Geosci. Remote Sens.*, **99**, 10.1109/TGRS.2013.2251639.
- Tanelli, S., S. Durden, E. Im, K. Pak, D. Reinke, P. Partain, J. Haynes, and R. Marchand, 2008: CloudSat’s Cloud Profiling Radar After 2 Years in Orbit: Performance, Calibration, and Processing. *IEEE Trans. Geosci. Remote Sens.*, **46** (11), 3560–3573.
- Tanelli, S., E. Im, S. L. Durden, L. Facheris, and D. Giuli, 2002: The effects of nonuniform beam filling on vertical rainfall velocity measurements with a spaceborne Doppler radar. *J. Atmos. Ocean Technol.*, **19** (7), 1019–1034, doi: 10.1175/1520-0426(2002)019.
- Tanelli, S., E. Im, S. R. Mascelloni, and L. Facheris, 2005: Spaceborne Doppler radar measurements of rainfall: correction of errors induced by pointing uncertainties. *J. Atmos. Ocean Technol.*, **22** (11), 1676–1690, doi: 10.1175/JTECH1797.1.

The Decadal Survey, (Ed.) , 2017: *Thriving on Our Changing Planet: A Decadal Strategy for Earth Observation from Space*. The National Academies Press.

Venema, V., S. G. Garcia, and C. Simmer, 2010: A new algorithm for the downscaling of cloud fields. *Quart. J. Roy. Meteor. Soc.*, **136**, 91–106, doi:10.1002/qj.535.

5 Wolde, M., A. Battaglia, C. Nguyen, A. L. Pazmany, and A. Illingworth, 2018: Implementation of Polarization Diversity Pulse Pair Technique using airborne W-band radar. *Atm. Meas. Tech. Disc.*, submitted.

Zeng, X., S. Ackerman, R. D. Ferraro, T. J. Lee, J. Murray, S. Pawswson, C. Reynoldsldslds, and J. Teixeira, 2016: Challenges and opportunities in NASA weather research. *Bull. Amer. Met. Soc.*, <https://doi.org/10.1175/BAMS-D-15-00195.1>.